A Dead-Time Compensation Strategy Based on an Online Learned Artificial Neural Network

Ludek Buchta, Matus Kozovsky, and Petr Blaha

***Abstract*—This article presents an innovative approach to mitigate the harmonic distortion of the phase currents of a permanent magnet synchronous motor (PMSM) controlled by a field-oriented control (FOC) algorithm. The issue of phase current harmonic distortion is often a consequence of the output voltage deformation caused by the nonlinearities of the voltage source inverter (VSI). The relationship between the disturbance voltages of the inverter and the phase currents of the motor is nonlinear. Therefore, we used an artificial neural network (ANN) to identify the compensation voltages. The topology is designed to allow the neural network to solve complex problems with the limited computing resources available on the AURIX TC397 microcontroller. The input vector is assembled from quantities available in the PMSM FOC algorithm. The online learning process based on the backpropagation algorithm is adapted to operate directly on the microcontroller. The proposed strategy with ANN is verified on a real PMSM. The results show the excellent ability of the proposed ANN to suppress the harmonic distortion of the PMSM phase currents without knowledge of the VSI parameters.**

***Index Terms*—Artificial neural network (ANN), dead-time effect, inverter nonlinearities compensation, permanent magnet synchronous motor (PMSM), voltage source inverter (VSI).**

I. Introduction

VOLTAGE source inverters (VSIs) are widely used to control electrical drives due to their high efficiency and ease of deployment in industrial applications. The high efficiency and precise application of the control values are required from the control algorithms. Achieving these requirements is complicated by VSI nonlinearities, including the dead-time period, snubber and parasitic capacitance, and voltage drops on the switching elements and antiparallel diodes. These nonlinearities cause a difference between the reference voltage calculated by the control algorithm and the voltage applied to the motor. This difference causes harmonic distortion of the phase currents, which leads to torque pulsations and adversely affects the efficiency of the control algorithm [1]. Therefore, it is recommended that a compensation strategy for VSI nonlinearities be integrated into the control algorithm.

The basic form of the compensation strategy is the feedforward approach [2], [3], which compensates the average voltage losses of one pulse-width modulation (PWM) period based on the polarities of the phase currents. This approach has two main weaknesses: the inaccurate model of the compensation voltages and the dependence on the accurate polarity detection of the phase currents. The detection of the current polarity is essential in zero-crossing regions [4], [5], [6], [7].

The strategies based on the mathematical model description of the VSI output voltages are presented in [8], [9], [10], and [11]. In [8], the compensation method involves calculating and injecting sinusoidal voltages at the frequencies of the parasitic harmonics into the output voltages. However, this approach reaches its limitations during load torque transients. The mathematical models, including the parasitic capacitance, are presented in [9], [10]. In [9], precise equations are used for the online calculation of the compensation voltage based on measured phase currents and VSI parameters, while [10] uses look-up tables for the calculation. The article [11] introduces the technique of trapezoidal voltage compensation, which controls the angle and amplitude of the output voltage. However, all three methods in [9], [10], and [11] rely on accurate measurement of the phase currents and precise knowledge of the VSI parameters, which vary with the operating conditions of the motor and the temperature of the power components.

The authors in [12], [13], and [14] employ the elements of artificial neural networks (ANNs) more frequently to mitigate VSI voltage distortions. The concept in [12] utilized a simple ANN to identify nonlinear compensation voltages, applying the deviation from the circular trajectory of the voltage vector in $\alpha\beta$-coordinates to create an adaptation rule to adjust a single weight in the input layer of the ANN. The drawback is the necessity to calculate the maximum value of the dead-time compensation voltage by measuring the current and voltage in the $\alpha\beta$-coordinates. In addition, the ANN only adjusts one weight, while the others remain fixed. In [13], eight individual neurons allow compensating for the 6th and 12th harmonics of the dq-currents. The amplitudes of the sine and cosine

Received 8 August 2024; revised 23 November 2024 and 22 January 2025; accepted 4 February 2025. Date of publication 3 April 2025; date of current version 5 September 2025. This work was supported in part by the project Archimedes: Trusted lifetime in operation for a circular economy under Grant 101112295/9A23010, in part by the Ministry of Education, Youth and Sports of the Czech Republic and Chips Joint Undertaking, in part by the infrastructure of RICAIP through European Union's Horizon 2020 research and innovation program under Grant 857306, and in part from the Ministry of Education, Youth and Sports under OP RDE under Grant CZ.02.1.01/0.0/0.0/17_043/0010085. *(Corresponding author: Ludek Buchta.)*

The authors are with the Central European Institute of Technology, Brno University of Technology, 61200 Brno, Czech Republic (e-mail: Ludek.Buchta@ceitec.vutbr.cz; Matus.Kozovsky@ceitec.vutbr.cz; Petr.Blaha@ceitec.vutbr.cz).

Digital Object Identifier 10.1109/TIE.2025.3544207

signal components for the compensated harmonics are adjusted through the adaptation rule. In [14], the authors proposed an algorithm with adaptive-linear-neurons for both the estimation and the compensation of only the sixth harmonics contained in dq-currents. However, the authors in all three articles do not fully utilize the potential of neural networks to identify the nonlinear compensation voltages.

In [15] and [16], the authors used different filters to extract harmonics from the currents, but these filters require adjustment according to the motor speed. In [15], an adaptive second-order filter was designed to extract the sixth harmonics of the dq-currents. The filtered sixth harmonics and the mathematical model of the permanent magnet synchronous motor (PMSM) facilitate calculating the compensation voltages. However, the higher parasitic harmonics are not compensated.

The different observers based on the mathematical motor model designed to compensate for the VSI nonlinearities are presented in [1], [17], and [18]. The observers typically rely on the accuracy of the motor model and its parameter knowledge.

In the article [16], the authors proposed a harmonic controller to deal with the six most significant harmonics caused by the dead-time effect. The harmonic current controller is divided into different parts and implemented in coordinate systems related to each harmonic component. However, accurate processing of the 17th and 19th harmonics is complicated at higher motor speeds. In [19], the authors proposed a compensation strategy that calculates the compensation voltage amplitude based on voltage differences after current injection.

In this article, a compensation strategy based on the online trained ANN is proposed to mitigate the harmonic distortion of the phase currents of the PMSM by adding compensation voltages to the control voltages. The ANN topology is designed to balance the complexity required to approximate the nonlinear compensation voltages and the available computational resources. The compensation algorithm is implemented with the field-oriented control (FOC) algorithm on one core of the AURIX TC397 microcontroller, and it has been adapted for online learning during PMSM operation. The update of the ANN weights is calculated during each PWM period. Experiments on the real PMSM validate the effectiveness of the proposed compensation strategy with the ANN.

The article is structured as follows. Section II focuses on harmonic analysis of the nonlinear relationship between the compensation voltages and phase currents. Section III presents the proposed ANN-based compensation strategy, including the ANN topology design and the online learning approach. Section IV then details the ANN implementation on the microcontroller, Section V presents the experimental validation, and Section VI summarizes the results.

II. Analysis of Voltage Disturbance

The dead-time issue can be demonstrated using the ι-phase leg (where: $\iota = a, b, c$) of the three-phase VSI, as shown in Fig. 1(a). This simplified analysis illustrates how the dead-time effect affects the VSI when insulated gate bipolar transistors

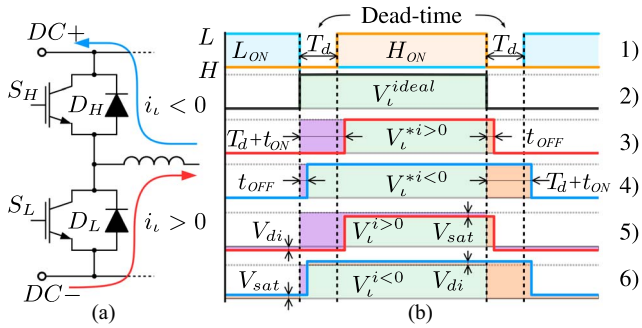

Fig. 1. (a) Single-phase leg during the dead-time period. (b) PWM patterns and VSI output voltages caused by the dead-time.

(IGBTs) are used as the switching devices. The dead-time period T_d is a short delay that is included in the PWM control signals of the switching devices. This delay is set to protect against short circuits in the same leg of the VSI. During the dead-time period T_d, the switching devices S_H and S_L are turned off, creating a brief moment when the output voltage is not under control. As a result, the phase current i_ι flows through the antiparallel diode D_H or D_L, depending on the polarity of the current. This results in a distortion of the VSI output voltage [2], shown in Fig. 1(b). The PWM patterns L/H with the dead-time period T_d are shown in waveform 1). The ideal VSI output voltage V_ι^{ideal} is in waveform 2), and the voltage V_ι^*, which includes the turn-ON t_{ON} and turn-OFF t_{OFF} delay times, is shown in waveforms 3)–4). The average voltage error ΔV_ι^* over one switching period T_{PWM} can be expressed [20] based on one inverter leg analysis as

$$\Delta V_\iota^* = V_d^* \operatorname{sign}(i_\iota) = \frac{T_d + t_{\text{ON}} - t_{\text{OFF}}}{T_{\text{PWM}}} V_{DC} \operatorname{sign}(i_\iota) \tag{1}$$

where V_{DC} denotes the dc bus voltage, and the sign function of the ι-phase current i_ι can be denoted as $\operatorname{sign}(i_\iota) = |i_\iota|/i_\iota$.

The resulting voltage error ΔV_ι is also affected by the switching devices conduction voltage drop V_{sat} and forward voltage drop of the antiparallel diodes V_{di}, as shown in Fig. 1(b) in 5)–6). The voltage error V_d is conventionally approximated with respect to the voltage drops [3] as

$$V_d = \frac{T_d + t_{\text{ON}} - t_{\text{OFF}}}{T_{\text{PWM}}} (V_{DC} - V_{\text{sat}} + V_{di}) + \frac{V_{\text{sat}} + V_{di}}{2}. \tag{2}$$

The voltage drops V_{sat} and V_{di} cannot be ignored, especially for a low dc bus voltage. We have $V_{\text{sat}} = V_{\text{sat0}} + |i_\iota| R_t$, $V_{di} = V_{di0} + |i_\iota| R_{di}$. The voltage drops consist of two parts: V_{sat0} and V_{di0} represent the threshold voltages; $|i_\iota| R_t$ and $|i_\iota| R_{di}$ stand for the ohmic losses, where R_t is the switcher resistance; and R_{di} denotes the diode forward resistance.

A. Harmonic Analysis

Undesirable voltage distortion is also transformed to the $\alpha\beta$- and dq-coordinate systems, as shown by harmonic analysis for a balanced PMSM [21]. The Clarke transformation can transform the voltage error ΔV_ι of all three phases ($\iota = a, b, c$)

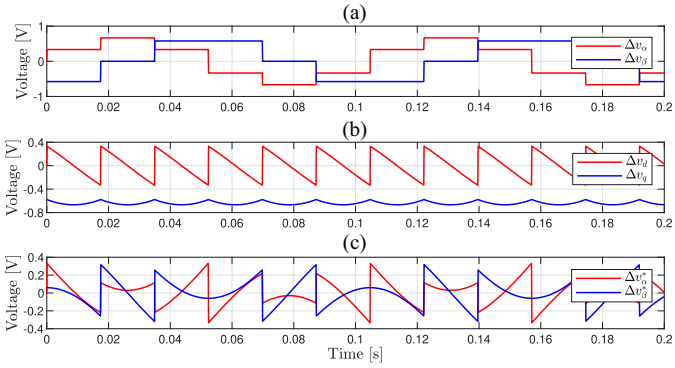

Fig. 2. Voltage distortions in the $\alpha\beta$- and dq-coordinates ($\gamma = 0$). (a) $\Delta \mathrm{v}_{\alpha\beta}$. (b) $\Delta \mathrm{v}_{dq}$. (c) $\Delta \mathrm{v}^*_{\alpha\beta}$.

into an $\alpha\beta$-stationary system, assuming negligible ohmic losses ($R_t, R_{di} = 0$) and constant V_d, as follows:

$$\begin{bmatrix}\Delta v_\alpha \\ \Delta v_\beta\end{bmatrix} = \frac{1}{3}\begin{bmatrix}2 & -1 & -1 \\ 0 & \sqrt{3} & -\sqrt{3}\end{bmatrix}\begin{bmatrix}V_d\,\mathrm{sign}(i_a) \\ V_d\,\mathrm{sign}(i_b) \\ V_d\,\mathrm{sign}(i_c)\end{bmatrix}. \tag{3}$$

The voltage errors Δv_α and Δv_β are expanded into the Fourier series [1]. After applying trigonometric functions, they can be represented as follows:

$$\Delta v_\alpha = \frac{4}{\pi}V_d\left(\sin(\varrho) + \sum_{n=1}^{+\infty}\left(\frac{\sin(\varrho\sigma^-)}{\sigma^-} + \frac{\sin(\varrho\sigma^+)}{\sigma^+}\right)\right) \tag{4}$$

$$\Delta v_\beta = \frac{4}{\pi}V_d\left(-\cos(\varrho) + \sum_{n=1}^{+\infty}\left(\frac{\cos(\varrho\sigma^-)}{\sigma^-} - \frac{\cos(\varrho\sigma^+)}{\sigma^+}\right)\right) \tag{5}$$

where: $\varrho = (\theta_e + \gamma)$; $\sigma^- = (6n-1)$; $\sigma^+ = (6n+1)$. The angle θ_e denotes the rotor electrical position of the rotor, while γ represents the angle between the current vector and the back electromotive force (back-EMF) voltage vector. Multiples of the $6n \pm 1$ harmonics cause voltage distortions. The 5th and 7th harmonics are dominant. The amplitude is dependent on the voltage error V_d. The curves of the $\Delta \boldsymbol{v}_{\alpha\beta}$ voltages are shown in Fig. 2(a). The voltage errors from (4)–(5) are transformed into dq-coordinates using the Park transformation, as follows:

$$\Delta v_d = \frac{4}{\pi}V_d\left(\sin(\gamma) + \sum_{n=1}^{+\infty}\left(\frac{\sin(\kappa-\gamma)}{6n-1} + \frac{\sin(\kappa+\gamma)}{6n+1}\right)\right) \tag{6}$$

$$\Delta v_q = \frac{4}{\pi}V_d\left(-\cos(\gamma) + \sum_{n=1}^{+\infty}\left(\frac{\cos(\kappa-\gamma)}{6n-1} - \frac{\cos(\kappa+\gamma)}{6n+1}\right)\right) \tag{7}$$

where: $\kappa = 6n(\theta_e + \gamma)$.

If the angle γ is zero or nearly zero, the disturbance voltage $\Delta \boldsymbol{v}_{dq}$ [Fig. 2(b)] depends solely on the rotation angle θ_e. The multiples of the sixth harmonics are dominant in this case. The voltages Δv^*_α and Δv^*_β represent exclusively the harmonic distortion components in the $\alpha\beta$-coordinates. These voltages are defined under the assumption that the angle γ is close to zero, and without containing fundamental harmonic components, expressed as follows:

$$\Delta v^*_\alpha = \frac{4}{\pi}V_d\sum_{n=1}^{+\infty}\left(\frac{\sin(\theta_e(6n-1))}{6n-1} + \frac{\sin(\theta_e(6n+1))}{6n+1}\right) \tag{8}$$

$$\Delta v^*_\beta = \frac{4}{\pi}V_d\sum_{n=1}^{+\infty}\left(\frac{\cos(\theta_e(6n-1))}{6n-1} - \frac{\cos(\theta_e(6n+1))}{6n+1}\right). \tag{9}$$

The curves of the $\Delta \boldsymbol{v}^*_{\alpha\beta}$ voltages are shown in Fig. 2(c). These voltage distortions (4)–(7) manifest themselves through the motor impedance as distortions of the $\alpha\beta$- and dq-currents at the same frequencies [14].

III. Compensation Strategy Design

The above analysis presents the main issues causing the distortion of the VSI output voltages. These voltage distortions can be described by the nonlinear functions (4)–(9). This fact leads us to use an ANN to deal with this nonlinear issue. We have established several requirements that need to be met in order to create a suitable ANN:

1) Accurate disturbance voltage approximation;
2) Availability of the input signals in the FOC algorithm;
3) Online learning capability;
4) Fast adaptation of the ANN to the new operating point; and
5) Suitability for microcontroller implementation.

A. Neural Network Topology Design

The voltages (8)–(9) represent mathematical expressions of nonlinear signals that the ANN-based strategy should learn to generate automatically based on the current operating conditions and the harmonic distortion of the measured phase currents. In a steady state, the nonlinear functions (8)–(9) are repeated at each electrical revolution. The maximum of the signals is defined by V_d in (2) and depends on the VSI parameters and the operating conditions. The voltage distortions change significantly faster than the phase currents.

The ability of an ANN to solve complex nonlinear problems depends on the number of hidden layers and neurons. Considering the properties of nonlinear signals, we chose the ANN topology (Fig. 3) with two hidden layers of 20 and 10 neurons, respectively. According to the universal approximation theorem [22], two hidden layers with enough neurons can approximate any nonlinearity. Adding more hidden layers would significantly increase the training time of the ANN. The number of neurons in the hidden layers was chosen experimentally as balance between the capability of the ANN topology to generate online compensation voltages and the limited computational resources available in the microcontroller. The two output neurons correspond to the $\alpha\beta$-coordinates where the compensation voltages are identified.

The selection of appropriate input signals that contain a significant amount of relevant information is a crucial aspect of the ANN design. The input vector $\boldsymbol{x}$ contains eight signals that

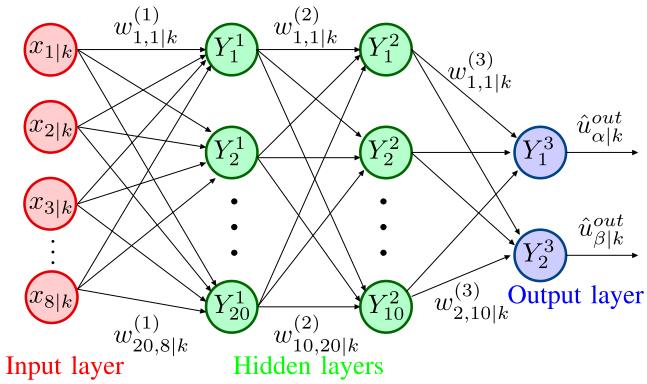

Fig. 3. Topology of the designed neural network.

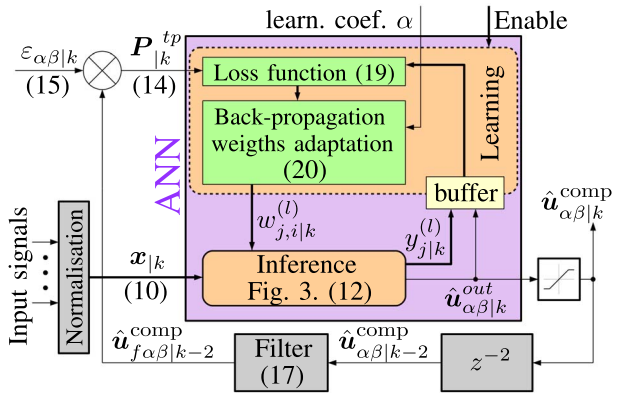

Fig. 4. Block diagram of the proposed ANN-based comp. strategy.

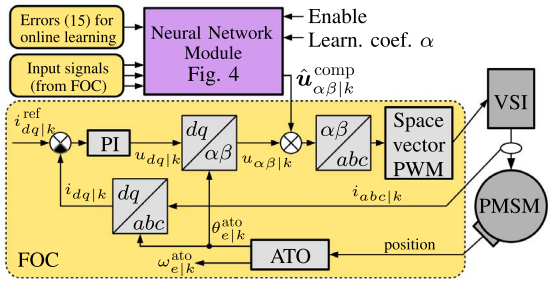

Fig. 5. Block diagram of the FOC with compensation strategy.

are directly available in the FOC algorithm or can be easily calculated. The input vector $\boldsymbol{x}$ is defined as

$$\boldsymbol{x} = \left[i_a^n, i_b^n, i_c^n, I_{\text{amp}}^n, \gamma, \omega_e^{n,\text{ato}}, \sin(6\theta_e^{\text{ato}}), \cos(6\theta_e^{\text{ato}})\right]^T \quad (10)$$

$$\boldsymbol{i}_{abc}^n = \frac{\boldsymbol{i}_{abc}}{I_{\text{amp}}}, \quad I_{\text{amp}} = \sqrt{i_a^2 + i_b^2 + i_c^2}, \quad I_{\text{amp}}^n = \frac{I_{\text{amp}}}{I_{\text{max}}}. \quad (11)$$

We have chosen to use the normalized values of the phase currents (i_a^n, i_b^n, i_c^n) as the input signals because the phase currents are measured directly, and their shapes contain regions, where the currents pass through zero values. The phase current values are normalized in the range $\langle -1, 1\rangle$ using (11). The following input is the normalized value of the current vector I_{amp}^n in the range $\langle 0, 1\rangle$, which ensures a faster response of the ANN to a change in the torque. The constraint I_{max} is given by the maximum current of the motor (6 A in our case).

The γ angle is obtained from the dq-currents because the back-EMF voltage vector is aligned with the q-axis. The dead-time effect and other VSI nonlinearities cause the ripples in the angle γ. This error carries information about persistent harmonic distortion, which the ANN can use to compensate for the VSI nonlinearities. Another input is the normalized value of the velocity $\omega_e^{n,\text{ato}}$ in the range $\langle -1, 1\rangle$, which allows the ANN to quickly adapt to velocity changes. The electrical position θ_e^{ato} and the velocity ω_e^{ato} are estimated by the angle tracking observer (ATO). The last pair of input signals $\sin(6\theta_e^{\text{ato}})$ and $\cos(6\theta_e^{\text{ato}})$ represent the sine and cosine functions of six times the estimated electrical position θ_e^{ato}.

The basic element of the mathematical model of the ANN is a neuron. The following equation defines the output $y_j^{(l)}$ of the neuron $Y_j^{(l)}$ in the lth layer as:

$$y_{j|k}^{(l)} = f\left(b_{j|k}^{(l)} + \sum_{i=1}^{m} w_{j,i|k}^{(l)} y_{i|k}^{(l-1)}\right). \quad (12)$$

The symbol j denotes the jth neuron in the layer. The output of the neuron $Y_i^{(l-1)}$ from the previous layer is represented as $y_i^{(l-1)}$. If the previous layer is the input layer, the previous outputs are replaced by the inputs x_i from the input vector $\boldsymbol{x}$. The weights for the jth neuron are represented by $w_{j,i}^{(l)}$, and the bias for that neuron is represented by $b_j^{(l)}$. The function $f(\chi)$ represents the activation function for a given neuron as

$$f_{\tanh}(\chi) = \tanh(\chi), \quad f'_{\tanh}(\chi) = 1 - \tanh^2(\chi). \quad (13)$$

Selecting suitable activation functions $f(\chi)$ is essential for the design of the ANN. We have chosen the hyperbolic tangent $f_{\tanh}(\chi)$ for the input and hidden layers, and a linear function $f_{\text{out}}(\chi) = \chi$ with derivative $f'_{\text{out}}(\chi) = 1$ for the output layer.

B. Neural Network Inference and Online Learning

The motivation for using online learning is the benefit of introducing feedback into the VSI disturbance voltage compensation process that would not be available in an offline learning approach. The block diagram of the proposed compensation strategy with the ANN is shown in Fig. 4, while its integration into the FOC is shown in Fig. 5. During PMSM operation with active online learning, the inference and learning take place in the following steps.

1) Training Pattern: In order to implement our proposed concept of online learning, it is necessary to create a new training pattern $\boldsymbol{P}_k^{tp} = [u_{\alpha|k}^{tp}, u_{\beta|k}^{tp}]^T$ at every step of the learning process. The training pattern is computed by summing the previous filtered ANN outputs obtained from ANN feedback (as shown in Fig. 4) with errors $\varepsilon_{\alpha|k}$ and $\varepsilon_{\beta|k}$, as follows:

$$\begin{bmatrix} u_{\alpha|k}^{tp} \\ u_{\beta|k}^{tp} \end{bmatrix} = \begin{bmatrix} \hat{u}_{f\alpha|k-2}^{\text{comp}} \\ \hat{u}_{f\beta|k-2}^{\text{comp}} \end{bmatrix} + \begin{bmatrix} \varepsilon_{\alpha|k} \\ \varepsilon_{\beta|k} \end{bmatrix} \quad (14)$$

where errors $\varepsilon_{\alpha|k}$ and $\varepsilon_{\beta|k}$ are calculated based on the phase currents $\boldsymbol{i}_{abc|k}$ measured in step k. These errors indicate the feedback from the residual harmonic distortion that has not been fully suppressed by the compensation voltages calculated two steps earlier in the compensation algorithm. Therefore, in (14), these errors are added to the compensation voltages in step $k-2$ to iteratively form an optimal training pattern for ANN. The errors $\varepsilon_{\alpha|k}$ and $\varepsilon_{\beta|k}$ are determined as

$$\begin{bmatrix}\varepsilon_{\alpha|k}\\ \varepsilon_{\beta|k}\end{bmatrix} = \boldsymbol{T}_{p|k}^{-1}\boldsymbol{K}_{\text{gain}}\left(\begin{bmatrix}i_{d|k}^{\text{ref}}\\ i_{q|k}^{\text{ref}}\end{bmatrix} - \begin{bmatrix}i_{d|k}\\ i_{q|k}\end{bmatrix}\right) \tag{15}$$

where $i_{d|k}^{\text{ref}}$ and $i_{q|k}^{\text{ref}}$ represent the dq-current setpoints, and $i_{d|k}$ and $i_{q|k}$ are the measured currents. The differences between the currents are multiplied by the correction gain $\boldsymbol{K}_{\text{gain}}$ that corresponds to the R_s stator resistance of the PMSM. The symbol $\boldsymbol{T}_p^{-1}$ denotes the inverse Park-transformation matrix from dq- to $\alpha\beta$-coordinates according to

$$\boldsymbol{T}_p = \begin{bmatrix}\cos(\theta_e^{\text{ato}}) & \sin(\theta_e^{\text{ato}})\\ -\sin(\theta_e^{\text{ato}}) & \cos(\theta_e^{\text{ato}})\end{bmatrix},$$

$$\boldsymbol{T}_p^{-1} = \begin{bmatrix}\cos(\theta_e^{\text{ato}}) & -\sin(\theta_e^{\text{ato}})\\ \sin(\theta_e^{\text{ato}}) & \cos(\theta_e^{\text{ato}})\end{bmatrix}. \tag{16}$$

The ANN outputs $\hat{u}_{\alpha|k-2}^{\text{comp}}$ and $\hat{u}_{\beta|k-2}^{\text{comp}}$ in (14) are filtered in dq-coordinates according to

$$\begin{bmatrix}\hat{u}_{f\alpha|k-2}^{\text{comp}}\\ \hat{u}_{f\beta|k-2}^{\text{comp}}\end{bmatrix} = \boldsymbol{T}_{p|k-2}^{-1}F_f(q^{-1})\boldsymbol{T}_{p|k-2}\begin{bmatrix}\hat{u}_{\alpha|k-2}^{\text{comp}}\\ \hat{u}_{\beta|k-2}^{\text{comp}}\end{bmatrix} \tag{17}$$

$$F_f(q^{-1}) = 1 - K_f\frac{b_f q^{-1}}{1-a_f q^{-1}} \tag{18}$$

where symbol q^{-1} denotes the backward shift operator. The parameters of the filter in (18) influence the feedback behavior of the ANN. For the learning process, the filter was configured with a gain of $K_f = 0.05$, constants $a_f = 0.9999$ and $b_f = 0.0001$, and a cutoff frequency of 1 rad/s.

The purpose of the filter $F_f(q^{-1})$ is to remove the dc components in the dq-coordinates that are represented by the terms $\sin(\gamma)$ and $-\cos(\gamma)$ in (6)–(7). This allows the ANN to learn how to compensate only harmonic distortions without interfering with the controllers. The control over the dc component of the dq-voltages is left only to PI current controllers, which is the standard in the FOC algorithm.

2) Learning Algorithm: The ANN learning algorithm is based on backpropagation [23] and stochastic gradient descent (SGD), which is modified for our online learning application. The backpropagation algorithm calculates the gradient of the loss function $E_{|k}$ with respect to each weight in the neural network, as follows:

$$E_{|k} = \frac{1}{2}\sum_{i=\{\alpha,\beta\}}^{n}\left(u_{i|k}^{tp} - \hat{u}_{i|k-2}^{\text{comp}}\right)^2. \tag{19}$$

The updates of the ith input weight of the jth neuron in the lth layer can be calculated as

$$w_{j,i|k}^{(l)} = w_{j,i|k-1}^{(l)} - \alpha\frac{\partial E_{|k}}{\partial w_{j,i|k-2}^{(l)}} \tag{20}$$

where α denotes the learning coefficient. The update of the biases $b_{j|k}^{(l)}$ for the current step k is calculated similarly.

The SGD adaptation method in (20) takes the gradients calculated by backpropagation and updates the weights $w_{j,i|k}^{(l)}$ accordingly. The individual steps described by these equations are essential to achieve correct feedback, which is not available in the earlier steps of the measured phase currents, and also to efficiently implement the learning algorithm on the microcontroller. The learning method can also be based on modifying the mini-batch SGD adaptation method. In this case, the mini-batch will represent data per one electrical revolution. This modification will improve the robustness of the learning but reduce the convergence speed.

3) Inference: The output for each layer is calculated according to (12) based on the current input vector (10) and updated weights according to (20). The ANN output is limited by saturation and set to the maximum value corresponding to the inverter parameters and the PMSM operation conditions. The resulting compensation voltages are added to the control values from the current PI controllers in $\alpha\beta$-coordinates as shown in Fig. 5.

IV. Implementation

The verification, integration, and implementation of the proposed ANN on the microcontroller involved three key steps. First, the ANN was designed and tested in MATLAB/Simulink to confirm that the proposed topology had sufficient hidden layers and neurons to ensure the necessary flexibility to solve the given task. In the second step, the ANN compensation strategy was integrated into the FOC algorithm. Then, the C code was automatically generated from MATLAB/Simulink. This approach effectively transfers the algorithm from the simulation environment to the microcontroller. In the final step, the generated code, together with the low-level drivers, was integrated into the final firmware and implemented on the Tricore AURIX TC397 microcontroller.

The six-core AURIX TC397 allocates only two cores to the control application: the FOC algorithm and the ANN-based proposed compensation strategy with the learning algorithm run on the first core at a sampling rate of 10 kHz, while the second core manages the data acquisition and communicates with MATLAB/Simulink via a user datagram protocol (UDP).

The effectiveness of the compensation strategy is evaluated on the test bench shown in Fig. 6. The FOC algorithm in AURIX TC397 generates PWM signals for the power inverter with IGBT switching elements, which control the three-phase PMSM TGT3. The PMSM is connected to a dynamometer, which serves as a speed reference. The main parameters of the VSI, PMSM, and FOC are listed in Table I. The current PI controllers used in FOC were designed conservatively.

Ensuring an acceptable computational complexity is one of the key requirements for implementing a compensation strategy in a microcontroller. The computational complexity has been measured on the AURIX TC397 and, for comparison, on the mainstream STM32G474RE microcontroller. The results are presented in Table II. The learning phase of the ANN is the most resource-intensive. After approximating the tanh

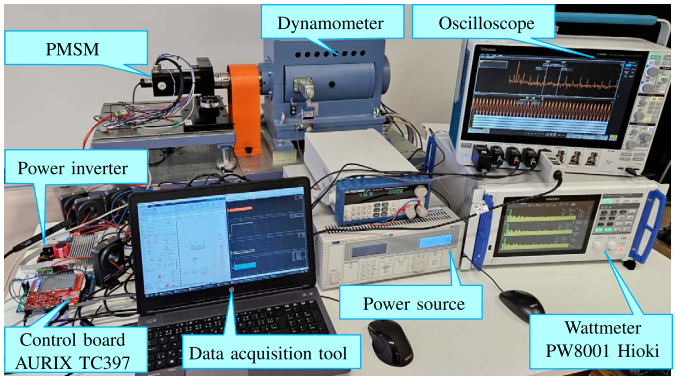

Fig. 6. Configuration of the testing platform.

TABLE I
PARAMETERS OF THE VSI, PMSM, AND FOC

Symbol	Quantity	Value
V_{DC}	DC voltage	$50\,V$
T_d	Dead-time period	$2\,\mu s$
V_{sat}	Switching device voltage drop	$1.5\,V$
V_d	Diode voltage drop	$1.7\,V$
P_N	Nominal power	$180\,W$
$i_{\max}$	Maximum motor current	$6\,A$
ω_r^N	Nominal speed	1500 rpm
p_p	Pole pairs	3
λ_m	Back-EMF constant	$0.0299\,Vs/\text{rad}$
R_s	Stator resistance	$0.5\,\Omega$
L_d	Direct inductance	$430\,\mu H$
L_q	Quadrature inductance	$450\,\mu H$
K_{dq}^{PI}	Gain of PI current controllers	$1.6\,V/A$
Ki_{dq}^{PI}	Integral constant of PI current controllers	1200 Hz

TABLE II
ANN COMPUTATION COMPLEXITY

Microcontroller	Inference	Learn. + Infer.
Aurix TC397	54 μs	72 μs
Aurix TC397 (tanh aprox.)	15 μs	33 μs
STM32G474	55.6 μs	95.2 μs
STM32G474 (tanh aprox.)	27.5 μs	67.1 μs

activation functions using a look-up table, the inference and learning phase takes an acceptable 33 μs on the AURIX TC397. The FOC algorithm requires an average of 7 μs for the computation, and an additional 5 μs is spent on measuring phase currents and configuring PWM peripheral registers.

To evaluate the progress of the online ANN learning process and the subsequent progress in the efficiency of the compensation of the VSI nonlinearities, the criterion C_{6h} is defined in (21). It indicates persistent harmonic distortion based on the quantities available in the FOC. The C_{6h} represents the sum of the magnitudes of the current vectors of the sixth harmonics in the d and q axes. The updating of the criterion C_{6h} is related

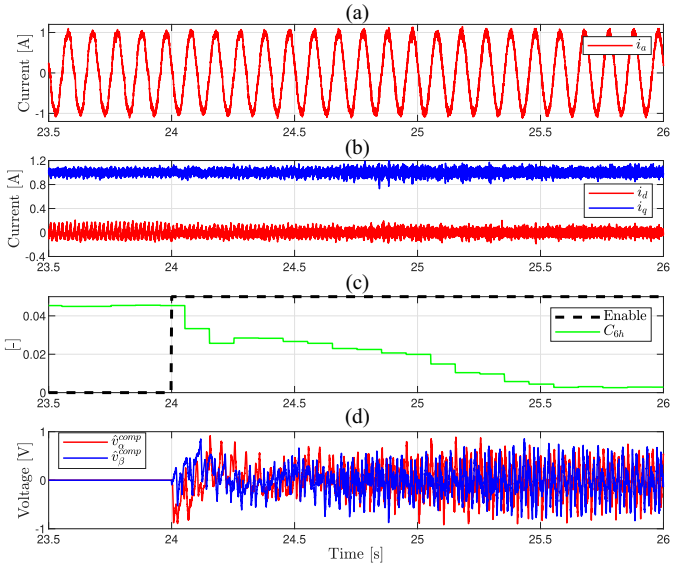

Fig. 7. Online learning process of the ANN and identification of the compensation voltages on real PMSM (data recorded via UDP). (a) Current i_a. (b) Current i_{dq}. (c) Enable ANN learning. (d) Compensation voltage $\hat{v}_{\alpha\beta}^{\text{comp}}$.

to the electrical rotation frequency of the PMSM as follows:

$$\begin{bmatrix} s_d^{6\theta_e} & c_d^{6\theta_e} \\ s_q^{6\theta_e} & c_q^{6\theta_e} \end{bmatrix} = \frac{1}{N}\sum_{k=1}^{N} \begin{bmatrix} i_d(k) \\ i_q(k) \end{bmatrix} \begin{bmatrix} \sin(6\theta_e^{\text{ato}}(k)) \\ \cos(6\theta_e^{\text{ato}}(k)) \end{bmatrix}^T \tag{21}$$

$$C_{6h} = \sqrt{{s_d^{6\theta_e}}^2 + {c_d^{6\theta_e}}^2 + {s_q^{6\theta_e}}^2 + {c_q^{6\theta_e}}^2} \tag{22}$$

where $s_d^{6\theta_e}$ and $c_d^{6\theta_e}$ denote the x- and y-coordinates of the current vector causing the 6th harmonic in the d-component, and $s_q^{6\theta_e}$ and $c_q^{6\theta_e}$ denote the coordinates of the q-component. The symbol N represents the number of samples per one electrical revolution.

V. EXPERIMENTS

This chapter describes the results of the experiments performed on the testbed in Fig. 6. The data from the experiments were recorded directly from the AURIX TC397 using the UDP communication interface and analyzed in MATLAB/Simulink on a PC. The total harmonic distortion (THD) of the phase currents was measured using the Hioki PW8001 wattmeter. We have configured the testbed for ANN learning with respect to the manifestation of the VSI nonlinearities. These are most noticeable in the measured quantities when the motor operates at a low speed and under low motor load. Therefore, the reference speed on the dynamometer was set to 200 rpm. The PMSM was run in the torque mode, and the setpoint of the q-current i_q^{ref} was set to 1 A. The experiments begin with the ANN in its initialization state, where all neurons across all layers are assigned default weights and biases. The weights for the first and second hidden layers are randomly initialized in the ranges $\langle -0.5, 0.5\rangle$ and $\langle -0.2, 0.2\rangle$, respectively, while the output layer weights are set in $\langle -0.1, 0.1\rangle$. The learning coefficient α was kept constant at 0.08.

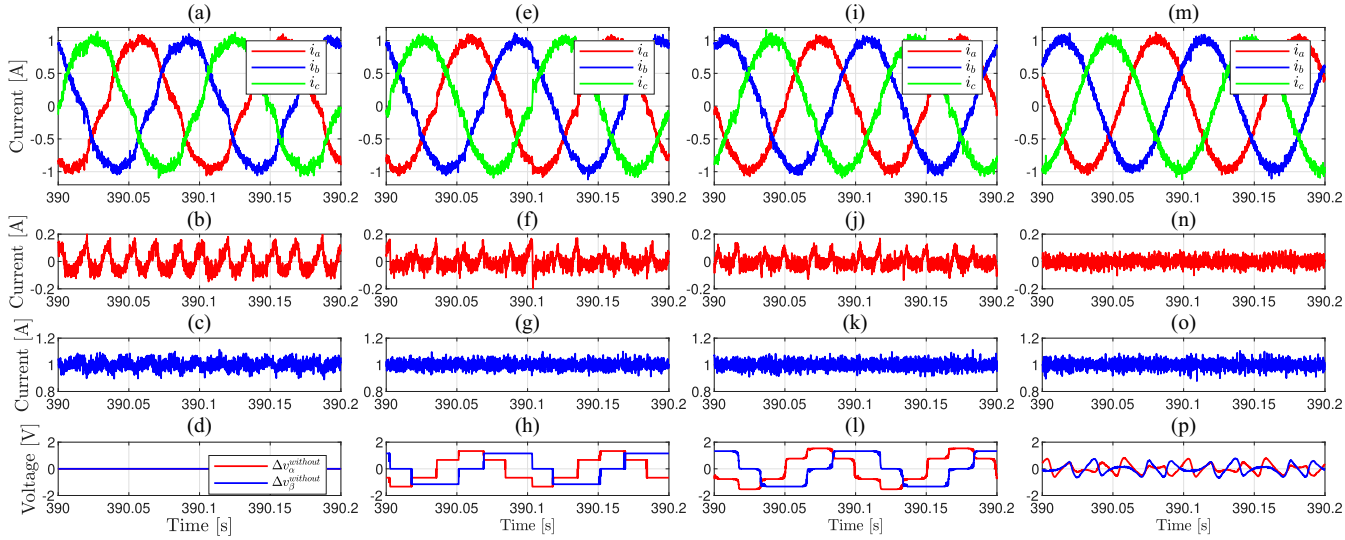

Fig. 8. Comparing experimental results: no comp., Sign comp., NDTC comp., and proposed ANN comp. at 200 rpm and i_q^{ref} 1 A (UDP data). (a) i_{abc} (without comp.). (b) Current i_d. (c) Current i_q. (d) Voltage $\Delta v_{\alpha\beta}^{\text{without}}$. (e) i_{abc} (Sign comp.). (f) Current i_d. (g) Current i_q. (h) Voltage $\Delta v_{\alpha\beta}^{\text{Sign}}$. (i) i_{abc} (NDTC comp.). (j) Current i_d. (k) Current i_q. (l) Voltage $\Delta v_{\alpha\beta}^{\text{NDTC}}$. (m) i_{abc} (ANN comp.). (n) Current i_d. (o) Current i_q. (p) Voltage $\hat{v}_{\alpha\beta}^{\text{comp}}$.

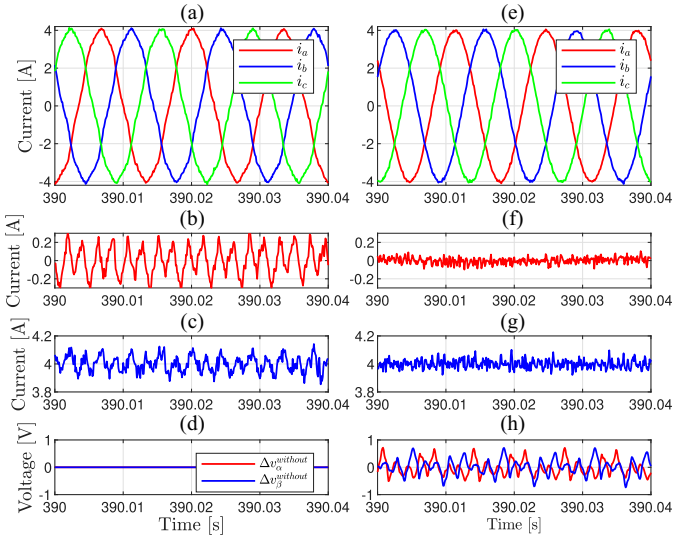

Fig. 9. Experimental results without comp. and with proposed ANN comp. under ref. speed 1500 rpm and i_q^{ref} 4 A (data recorded via UDP). (a) i_{abc} (without comp.). (b) Current i_d. (c) Current i_q. (d) Voltage $\Delta v_{\alpha\beta}^{\text{without}}$. (e) i_{abc} (ANN comp.) (f) Current i_d. (g) Current i_q. (h) Voltage $\Delta \hat{v}_{\alpha\beta}^{\text{comp}}$.

A. Online Learning Process

The online learning process of the ANN and the identification of the compensation voltages $\hat{\boldsymbol{u}}_{\alpha\beta}^{\text{comp}}$ started with an enable signal generated at the 24th second of the experiment, as shown in Fig. 7(c)–7(d). The progress in the online identification of the correct shape and size of the $\hat{\boldsymbol{u}}_{\alpha\beta}^{\text{comp}}$ is indicated by the decrease of the criterion C_{6h} in [Fig. 7(c)]. The value of the criterion is updated once per electrical revolution of the PMSM. After two seconds, the value of the criterion C_{6h} reaches almost zero. This means that the ANN has almost wholly suppressed the 6th harmonic component in the dq-currents. The progress of the compensation process is also documented by the gradual reduction of the harmonic distortion in the waveforms of the a-phase current and dq-currents, as shown in Fig. 7(a) and 7(b).

B. Comparing Compensation Approaches

The results of the proposed ANN-based strategy and comparisons with other compensation approaches are shown in Fig. 8. For comparison, two other compensation strategies were evaluated: the standard sign-based compensation method described by (2) and the nonlinear dead-time compensation (NDTC) method from [12], which is also an AI-based compensation strategy using simple ANN.

As a reference, the phase currents and dq-currents without applying any compensation strategy are shown in Fig. 8(a)–8(c). It is evident that the phase currents deviate from their ideal sinusoidal waveforms due to parasitic harmonic components and the zero-clamping phenomenon that occurs at zero-crossing regions. These distortions are also reflected in the dq-currents through transformations, causing them to ripple.

The application of the standard sign compensation strategy [Fig. 8(e)–8(g)] partially suppresses the harmonic distortions; the inaccurate detection of the phase current polarity limits its performance. This results in persistent distortion, particularly visible as peaks in the d-current near the zero-crossing regions of the phase currents.

The results of the NDTC method are shown in Fig. 8(i)–8(k). The NDTC outperforms the sign compensation strategy mainly by generating a smoother course of the compensation voltages without multiple level changes near zero-crossing regions. However, not even the NDTC is able to completely suppress the harmonic distortion in the d-current component.

The proposed ANN-based compensation strategy, shown in Fig. 8(m)–8(o), demonstrates the improvement in the ability to reduce harmonic distortion in both phase currents and

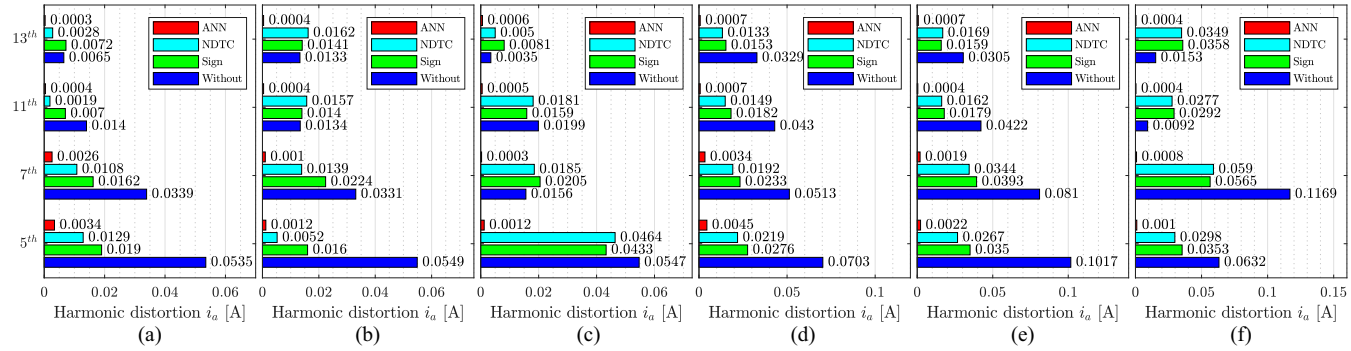

Fig. 10. Comparing the dominant 5th, 7th, 11th, and 13th parasitic harmonics of the a-phase currents under different operating conditions. (a) ω_r 200 rpm, i_q^{ref} 1 A. (b) ω_r 400 rpm, i_q^{ref} 1 A. (c) ω_r 1500 rpm, i_q^{ref} 1 A. (d) ω_r 200 rpm, i_q^{ref} 4 A. (e) ω_r 400 rpm, i_q^{ref} 4 A. (f) ω_r 1500 rpm, i_q^{ref} 4 A.

TABLE III
HARMONIC SUPPRESSION RATIO (HSR) OF THE DOMINANT HARMONICS (IN PERCENT)

	200 rpm, i_q^{ref} 1 A			400 rpm, i_q^{ref} 1 A			1500 rpm, i_q^{ref} 1 A			200 rpm, i_q^{ref} 4 A			400 rpm, i_q^{ref} 4 A			1500 rpm, i_q^{ref} 4 A		
Harm.	Sign	NDTC	ANN	Sign	NDTC	ANN	Sign	NDTC	ANN	Sign	NDTC	ANN	Sign	NDTC	ANN	Sign	NDTC	ANN
i_a 5th	64.53	75.79	93.58	70.78	90.44	97.77	20.89	15.26	97.88	60.71	68.79	93.55	65.58	73.74	97.88	44.20	52.79	98.43
i_a 7th	52.14	68.16	92.47	32.22	58.01	96.94	−31.27	−18.43	97.98	54.60	62.55	93.30	51.47	57.58	97.67	51.64	49.55	99.30
i_a 11th	49.63	86.17	96.93	−4.75	−17.60	96.97	20.16	8.86	97.46	57.70	65.44	98.35	57.56	61.56	99.04	−217.29	−200.68	95.13
i_a 13th	−10.03	57.48	95.70	−6.03	−22.26	97.08	−132.68	−44.89	81.64	53.40	59.66	97.89	47.83	44.51	97.84	−133.40	−127.46	97.07
i_d 6th	61.52	74.20	92.90	58.96	81.93	97.56	37.53	23.77	99.59	58.24	66.17	93.60	59.41	66.83	98.06	81.90	79.90	99.54
i_d 12th	37.52	90.07	95.30	−13.04	−26.33	99.37	50.26	20.60	96.78	56.79	64.87	97.89	55.16	57.47	98.75	−173.36	−163.36	98.01
i_q 6th	81.58	89.66	94.19	81.84	67.29	98.44	6.87	7.52	99.08	71.97	80.97	93.67	80.14	73.08	98.49	−59.12	−56.72	98.81
i_q 12th	68.38	74.52	98.17	51.07	84.05	94.10	−0.63	0.82	97.11	65.37	72.59	97.98	66.09	74.02	98.31	43.30	38.73	93.64

Note: The sign (−) indicates that the corresponding harmonic component has been amplified, not suppressed, by the specified percentage.

dq-currents, including in the challenging zero-crossing regions. The suppression of the current peaks is obvious in the d-current waveform in Fig. 8(n). The compensation voltages generated by the standard and NDTC strategies have a different shape compared to the voltages generated by the ANN, as shown in Fig. 8(h), 8(l), and 8(p) because the ANN is specifically self-trained to generate only the voltages necessary to suppress the harmonic distortions corresponding to Fig. 2(c).

The proposed ANN-based strategy was evaluated against other methods under different operating conditions, specifically at the setpoint q-current of 4 A and rotational speeds of 400 and 1500 rpm (PMSM nominal speed). The ANN-based compensation strategy effectively suppresses harmonic distortion in the phase currents and dq-currents, even at the higher speed of 1500 rpm, as is demonstrated in Fig. 9.

A detailed comparison of the suppression of the dominant harmonics in the a-phase current is shown in Fig. 10, proving that the ANN-based strategy effectively and consistently suppressed the dominant harmonics compared to alternative approaches. The dominant harmonics of the a-phase current (5th, 7th, 11th, and 13th) are represented in bar graphs. They are obtained from the measured data via UDP and processed in MATLAB using fast Fourier transform (FFT).

The harmonic suppression ratio (HSR) of the dominant harmonics in the a-phase current and dq-currents (dominant 6th and 12th harmonics) is presented in Table III as percentages.

TABLE IV
THD OF a-PHASE CURRENTS FROM WATTMETER (IN PERCENT)

	200 rpm		400 rpm		1500 rpm	
Method	i_q^{ref} 1 A	i_q^{ref} 4 A	i_q^{ref} 1 A	i_q^{ref} 4 A	i_q^{ref} 1 A	i_q^{ref} 4 A
Without	7.082	2.894	7.715	3.983	8.179	3.792
Sign	3.627	1.376	5.014	1.852	7.653	2.800
NTDC	3.097	1.219	4.413	1.597	7.480	2.712
ANN	2.082	0.515	2.793	0.646	6.635	1.491

The HSR is defined as

$$\text{HSR}_n = \left(1 - \left(I_n^{\text{comp}} / I_n^{\text{without}}\right)\right) 100 \tag{23}$$

where I_n^{without} is the magnitude of the nth harmonic component without compensation, and I_n^{comp} is its magnitude after compensation using one of the tested methods.

The FFT results in Fig. 10 and HSR in Table III clearly indicate that the NDTC method amplifies higher harmonic components under certain operating conditions. This observation is consistent with the results presented in [12], which demonstrate that NDTC amplifies the 13th harmonic when the frequency of the $\alpha\beta$-currents is approximately 11.6 Hz.

At higher motor speeds, both the sign-based and the NDTC methods struggle with the amplification of higher harmonics. This issue is particularly noticeable at the nominal motor speed

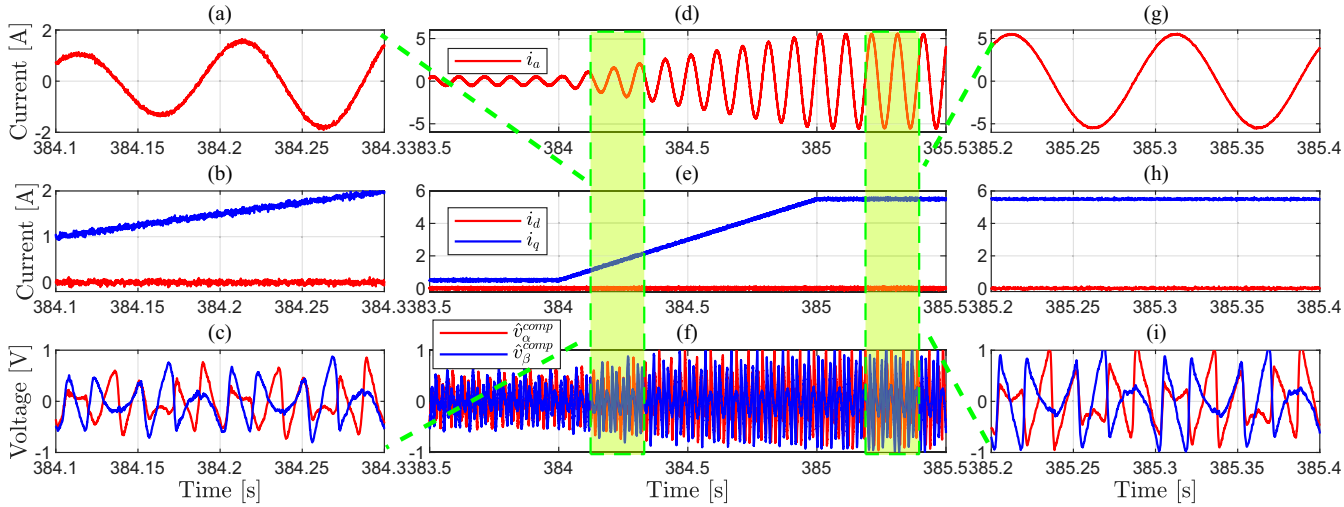

Fig. 11. Behavior of the proposed ANN comp. under torque ramp 0.5–5.5 A, reference speed 200 rpm (data recorded via UDP). (a) Detail i_a. (b) Detail i_{dq}. (c) Detail $\hat{v}_{\alpha\beta}^{\text{comp}}$. (d) Current i_a. (e) Current i_{dq}. (f) Comp. voltage $\hat{v}_{\alpha\beta}^{\text{comp}}$. (g) Detail i_a. (h) Detail i_{dq}. (i) Detail $\hat{v}_{\alpha\beta}^{\text{comp}}$.

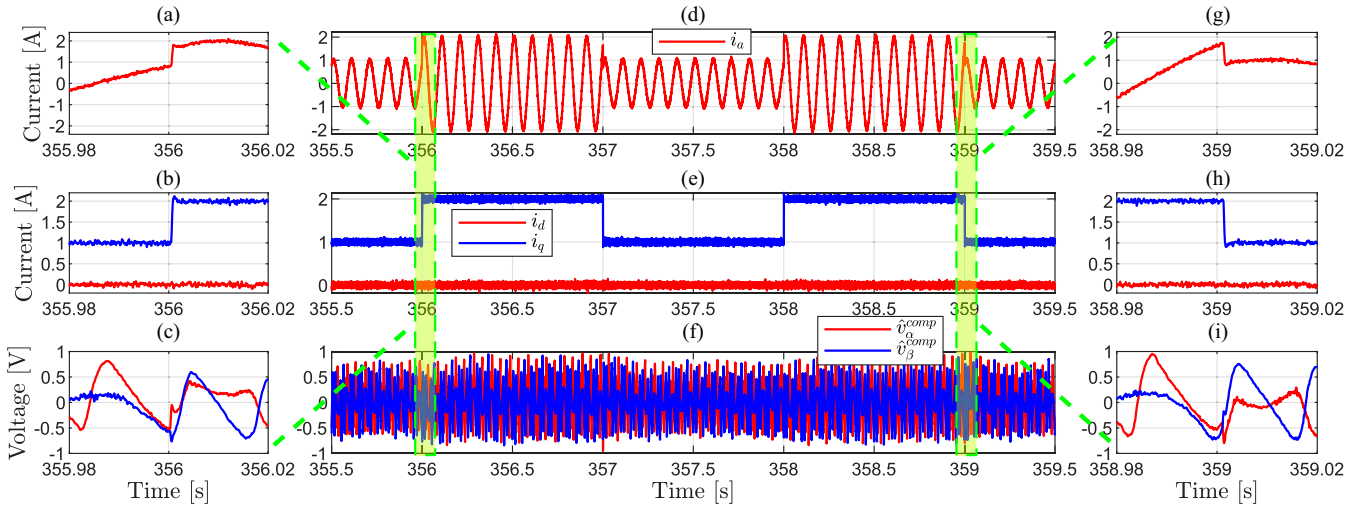

Fig. 12. Behavior of the proposed ANN comp. under q-current step response under reference speed 200 rpm (data recorded via UDP). (a) Detail i_a. (b) Detail i_{dq}. (c) Detail $\hat{v}_{\alpha\beta}^{\text{comp}}$. (d) Current i_a. (e) Current i_{dq}. (f) Compensation voltage $\hat{v}_{\alpha\beta}^{\text{comp}}$. (g) Detail i_a. (h) Detail i_{dq}. (i) Detail $\hat{v}_{\alpha\beta}^{\text{comp}}$.

of 1500 rpm, where both methods amplify the 13th harmonic of the i_q currents. Additionally, the 11th harmonic of the i_a is amplified by 200% at 1500 rpm and 4 A, mostly due to digital delays that diminish compensation accuracy.

The HSR results presented in Table III highlight the excellent and consistent performance of the ANN-based strategy compared to alternative approaches. These results prove that the proposed ANN does not amplify higher parasitic harmonics under the tested operating conditions but significantly suppresses them. All observed harmonics are suppressed by over 92%, except for 13th harmonic of the i_a at 1500 rpm and 1 A. It is important to note that the HSR of the individual harmonics is highly dependent on the operating conditions.

The Hioki PW8001 wattmeter measures the THD of individual PMSM phases; the THD is determined from the first 50 harmonic components. Table IV summarizes the a-phase THD values under tested operating conditions for evaluated strategies. The results show that the ANN-based strategy provides a notable improvement in THD reduction compared to the other methods.

C. Validating ANN Strategy During Transient States

The behavior of the trained ANN-based method during the transient was verified by the experiment in Fig. 11, where the q-current setpoint was gradually ramped from 0.5 to 5.5 A at a reference speed of 200 rpm. The detailed views in (a)–(c) show how the ANN responds to changes in operating conditions. As the q-current setpoint increases in Fig. 11(b), the amplitude of the phase currents increases accordingly, leading to higher ohmic losses in the switching elements and increased harmonic distortion. In response, the ANN increases the amplitude of the

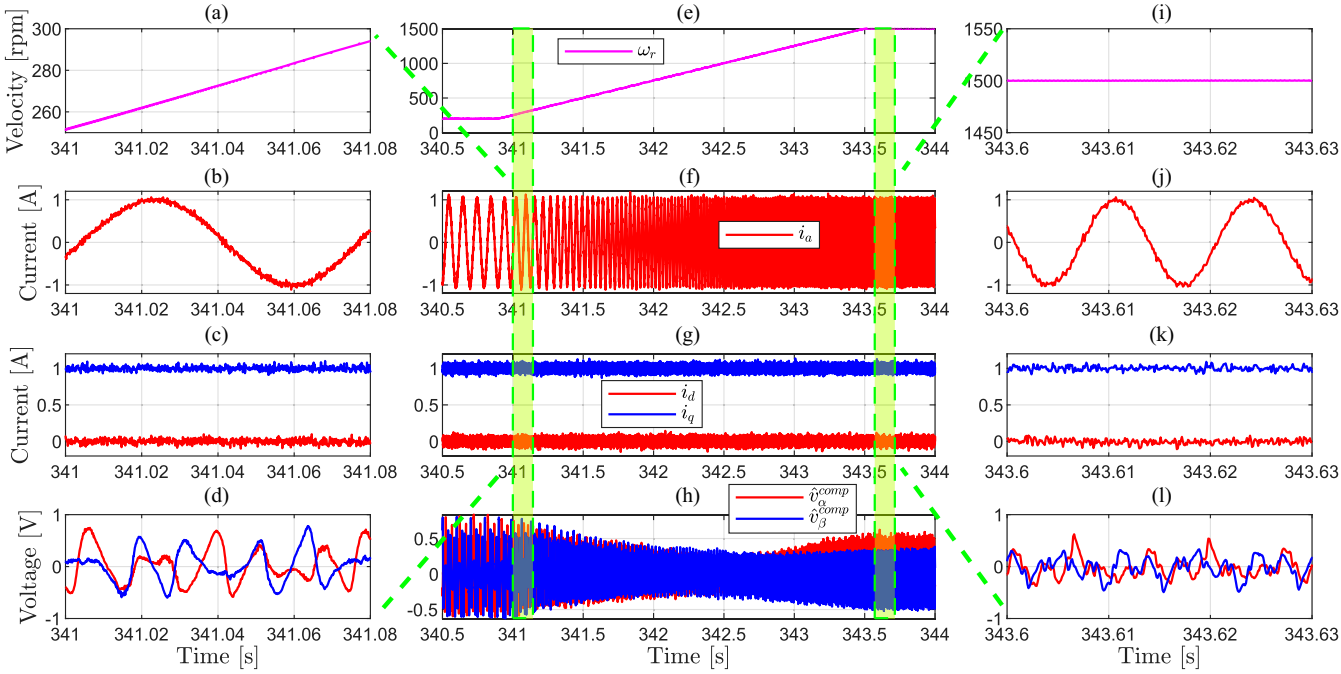

Fig. 13. Behavior of the proposed ANN comp. under velocity ramp 200–1500 rpm, current i_q^{ref} 1 A (data recorded via UDP). (a) Detail velocity ω_r. (b) Detail i_a. (c) Detail i_{dq}. (d) Detail $\hat{v}_{\alpha\beta}^{\text{comp}}$. (e) Velocity ramp ω_r. (f) Current i_a. (g) Current i_{dq}. (h) Comp. voltage. (i) Detail velocity ω_r. (j) Detail i_a. (k) Detail i_{dq}. (l) Detail $\hat{v}_{\alpha\beta}^{\text{comp}}$.

compensation voltages based on learned links between the input signals and the required compensation voltages. The ANN ensures consistent compensation quality throughout the transient state, as is shown in details (a)–(c) and (g)–(i) in Fig. 11.

In Fig. 12, the experiment evaluates the performance of the ANN during step changes in the q-current setpoint between 1 and 2 A at a reference speed of 200 rpm. The detailed waveforms in (a)–(c) and (g)–(i) demonstrate that the ANN responds immediately to variations in operating conditions while maintaining consistent compensation quality.

The final experiment under transient conditions evaluates the performance of the ANN during ramped speed transitions from 200 rpm to the nominal PMSM speed of 1500 rpm, with a constant q-current setpoint of 1 A, as illustrated in Fig. 13. The ANN-based compensation strategy dynamically adapts to the speed ramp by changing the amplitude and shape of the compensation voltages according to the learned connections within the ANN, ensuring consistent compensation quality. This adaptability is evident in the detailed waveforms shown in (a)–(d) and (i)–(l) in Fig. 13.

D. Challenges and Limitations of the ANN Implementation

The primary drawback of the proposed ANN-based approach is its higher computational complexity, requiring 33 μs compared to 2 μs for the NDTC method on the AURIX TC397 microcontroller. Another limitation of the proposed ANN approach is its dependence on the velocity estimated by the ATO as one of its inputs. The remaining inputs are derived from signals readily available only within the FOC algorithm. Another drawback of the proposed ANN method is the tendency to adapt too closely to one specific operating point. In this case, permanent learning can lead to forgetting the correct behavior at infrequently used operating points. This issue can be addressed by temporarily disabling the neural network training or dynamically adjusting the learning coefficient. All experiments were performed using a blank ANN with randomly initialized weights. Real applications may require pretraining of the ANN in simulations or using the nonvolatile memory of the microcontroller to store weights after adaptation to real hardware.

VI. Conclusion

This article addresses the challenges of mitigating distortion in the VSI output voltages by introducing an ANN-based compensation strategy. The ANN topology is designed to balance the complexity required to approximate the nonlinear compensation voltages with the computational constraints of the AURIX TC397 microcontroller and the online learning capability directly on the microcontroller. The experimental results demonstrate that the proposed strategy significantly reduces the current harmonic distortions caused by the dead-time effect and other VSI nonlinearities. The proposed approach outperforms the AI-based NDTC and the standard sign-based methods. The strategy reduced the THD of the a-phase current from 7.082% to 2.082%. The ANN demonstrates robust performance and maintains a consistent level of compensation under various operating conditions. The advantages of the proposed approach are its ability to identify compensation voltages online and the feasibility of implementing it on available microcontrollers at

the cost of an acceptable increase in computational complexity. The ANN method can also be utilized to find the optimal compensation voltage, which can be used later in low-cost microcontrollers as look-up tables or for further offline ANN design and training.

REFERENCES

[1] Z. Tang and B. Akin, "A new LMS algorithm based deadtime compensation method for PMSM FOC drives," *IEEE Trans. Ind. App.*, vol. 54, no. 6, pp. 6472–6484, Nov./Dec. 2018.

[2] S.-K. Sul, *Control of Electric Machine Drive Systems* (IEEE Press Series on Power Engineering), 1st ed. Wiley-IEEE Press, 2011.

[3] S.-Y. Kim, W. Lee, M.-S. Rho, and S.-Y. Park, "Effective dead-time compensation using a simple vectorial disturbance estimator in PMSM drives," *IEEE Trans. Ind. Electron.*, vol. 57, no. 5, pp. 1609–1614, May 2010.

[4] S. M. Seyyedzadeh and A. Shoulaie, "Accurate modeling of the nonlinear characteristic of a voltage source inverter for better performance in near zero currents," *IEEE Trans. Ind. Electron.*, vol. 66, no. 1, pp. 71–78, Jan. 2019.

[5] A. Sarathy and K. Vasudevan, "An investigation of current ripple prediction based dead time compensation using a simplified motor model for a VSI fed induction motor drive," in *Proc. IEEE Int. Conf. - PESGRE*, 2024, pp. 1–6.

[6] Y. Zhao, W. Qiao, and L. Wu, "Dead-time effect analysis and compensation for a sliding-mode position observer-based sensorless IPMSM control system," *IEEE Trans. Ind. Appl.*, vol. 51, no. 3, pp. 2528–2535, May/Jun. 2015.

[7] D. Wang, M. Wang, Y. Shen, Q. Li, and X. Liang, "Online feedback dead time compensation strategy for three-level T-type inverters," *IEEE Trans. Ind. Electron.*, vol. 67, no. 9, pp. 7260–7268, Sep. 2020.

[8] J. Ye et al., "An accurate dead time compensation method for SPWM voltage source inverters," *IEEE Trans. Power Electron.*, vol. 38, no. 4, pp. 4894–4908, Apr. 2023.

[9] Z. Zhang and L. Xu, "Dead-time compensation of inverters considering snubber and parasitic capacitance," *IEEE Trans. Power Electron.*, vol. 29, no. 6, pp. 3179–3187, Jun. 2014.

[10] C. Shang, M. Yang, J. Long, D. Xu, J. Zhang, and J. Zhang, "An accurate VSI nonlinearity modeling and compensation method accounting for DC-Link voltage variation based on LUT," *IEEE Trans. Ind. Electron.*, vol. 69, no. 9, pp. 8645–8655, Sep. 2022.

[11] L. Wang, J. Xu, Q. Chen, Z. Chen, and R. Huang, "An improved trapezoidal voltage method for dead-time compensation in three-phase voltage source converter," *IEEE Trans. Power Electron.*, vol. 37, no. 8, pp. 8785–8789, Aug. 2022.

[12] T. Liu, Q. Li, Q. Tong, Q. Zhang, and K. Liu, "An adaptive strategy to compensate nonlinear effects of voltage source inverters based on artificial neural networks," *IEEE Access*, vol. 8, pp. 129992–130002, 2020.

[13] X. Wang and H. Zhu, "Vibration compensation control of BPMSM with dead-time effect based on adaptive neural network band-pass filter," *IEEE Trans. Power Electron.*, vol. 37, no. 6, pp. 7145–7155, Jun. 2022.

[14] T. Qiu, X. Wen, and F. Zhao, "Adaptive-linear-neuron-based dead-time effects compensation scheme for PMSM drives," *IEEE Trans. Power Electron.*, vol. 31, no. 3, pp. 2530–2538, Mar. 2016.

[15] Z. Wu et al., "Dead-time compensation based on a modified multiple complex coefficient filter for permanent magnet synchronous machine drives," *IEEE Trans. Power Electron.*, vol. 36, no. 11, pp. 12979–12989, Nov. 2021.

[16] M. G. Joksimovic, E. Levi, and S. N. Vukosavic, "Near-complete suppression of harmonic currents in SPMSMs caused by back EMF and dead time," *IEEE Trans. Ind. Electron.*, vol. 70, no. 5, pp. 4472–4484, May 2023.

[17] W. Dafang, Y. Bowen, Z. Cheng, Z. Chuanwei, and Q. Ji, "A feedback-type phase voltage compensation strategy based on phase current reconstruction for ACIM drives," *IEEE Trans. Power Electron.*, vol. 29, no. 9, pp. 5031–5043, Sep. 2014.

[18] D.-M. Park and K.-H. Kim, "Parameter-independent online compensation scheme for dead time and inverter nonlinearity in IPMSM drive through waveform analysis," *IEEE Trans. Ind. Electron.*, vol. 61, no. 2, pp. 701–707, Feb. 2014.

[19] K. Yu and Z. Wang, "An online compensation method of VSI nonlinearity for dual three-phase PMSM drives using current injection," *IEEE Trans. Power Electron.*, vol. 37, no. 4, pp. 3769–3774, Apr. 2022.

[20] Y. Yang, K. Zhou, H. Wang, and F. Blaabjerg, "Analysis and mitigation of dead-time harmonics in the single-phase full-bridge PWM converter with repetitive controllers," *IEEE Trans. Ind. App.*, vol. 54, no. 5, pp. 5343–5354, Sep. 2018.

[21] Z. Tang and B. Akin, "Compensation of dead-time effects based on revised repetitive controller for PMSM drives," in *Proc. IEEE APEC*, May 2017, pp. 2730–2737.

[22] I. Goodfellow, Y. Bengio, and A. Courville, *Deep Learning (Adaptive Computation and Machine Learning series)*. Cambridge, MA, USA: MIT Press, 2016.

[23] W. Sun, J. Tang, and C. Bai, "Evaluation of university project based on partial least squares and dynamic back propagation neural network group," *IEEE Access*, vol. 7, pp. 69494–69503, 2019.

Ludek Buchta was born in Brno, Czech Republic, in 1987. He received the Ph.D. degree in cybernetics from Brno University of Technology, Brno, in 2019.

Currently, he is a Researcher with the Central European Institute of Technology, Brno University of Technology. His research interests include compensating the nonlinearity of voltage source inverters, implementing neural network algorithms, and developing advanced algorithms to control ac electric motors.

Matus Kozovsky was born in Bratislava, Slovak Republic, in 1991. He received the Ph.D. degree in cybernetics from Brno University of Technology, Brno, Czech Republic, in 2021.

Currently, he is a Software Development Researcher with the Central European Institute of Technology, Brno University of Technology. His research interests include fault-tolerant control of ac electric motors, high-speed control of electrical motors, and inverter SW improvements.

Petr Blaha received the M.Sc. and Ph.D. degrees in cybernetics from Brno University of Technology, Brno, Czech Republic, in 1996 and 2001, respectively.

Currently, he is a Senior Researcher with the Central European Institute of Technology, Brno University of Technology. His research interests include parameter identification, advanced control and diagnostics of ac electric motors, and fault-tolerant control of electrical motor drives.